Article

Enhancing Transparency in Non-Cubic Calcium Phosphate Ceramics: Effect of Starting Powder, LiF Doping, and Spark Plasma Sintering Parameters

Kacper Albin Prokop [1,2], Sandrine Cottrino [3], Vincent Garnier [3], Gilbert Fantozzi [3], Yannick Guyot [4], Georges Boulon [4] and Małgorzata Guzik [1,2,*]

1   Faculty of Chemistry, University of Wrocław, ul. F. Joliot-Curie 14, 50-383 Wrocław, Poland; kacper2311@gmail.com
2   Łukasiewicz Research Network—PORT Polish Center for Technology Development, ul. 147 Stabłowicka, 54-066 Wroclaw, Poland
3   Institut National des Sciences Appliquées Lyon, Universite Claude Bernard Lyon 1, CNRS, MATEIS, UMR5510, 69621 Villeurbanne, France; sandrine.cottrino@insa-lyon.fr (S.C.); gilbert.fantozzi@insa-lyon.fr (G.F.)
4   Institut Lumière Matière, Universite Claude Bernard Lyon 1, CNRS, UMR5306, 69100 Villeurbanne, France; yannick.guyot@univ-lyon1.fr (Y.G.); georges.boulon@univ-lyon1.fr (G.B.)
*   Correspondence: goguzik@poczta.fm; Tel.: +48-71-37-51-373

Abstract: Our objective is to achieve a new good-quality and mechanically durable high-transparency material that, when activated by rare earth ions, can be used as laser sources, scintillators, or phosphors. The best functional transparent ceramics are formed from high-symmetry systems, mainly cubic. Considering hexagonal hydroxyapatite, which shows anisotropy, the particle size of the initial powder is extremely important and should be of the order of several tens of nanometers. In this work, transparent micro-crystalline ceramics of non-cubic $Ca_{10}(PO_4)_6(OH)_2$ calcium phosphate were fabricated *via* Spark Plasma Sintering (SPS) from two types of nanopowders i.e., commercially available (COM. HA) and laboratory-made (LAB. HA) *via* the hydrothermal (HT) protocol. Our study centered on examining how the quality of sintered bodies is affected by the following parameters: the addition of LiF sintering agent, the temperature during the SPS process, and the quality of the starting nanopowders. The phase purity, microstructure, and optical transmittance of the ceramics were investigated to determine suitable sintering conditions. The best optical ceramics were obtained from LAB. HA nanopowder with the addition of 0.25 wt.% of LiF sintered at 1000 °C and 1050 °C.

Keywords: non-cubic calcium phosphates; nano-crystalline powders; SPS; transparency; optical material

1. Introduction

Over the past two decades, transparent ceramics have gained significant attention as advanced optical ceramic materials. Recently, the list of applications of transparent ceramics, for which some of them are highly sophisticated, for laser media, phosphors, scintillators, armor windows, infrared domes, and electro-optical components has widely increased in all domains and has impacted our daily lives [1–3]. They are recognized for their combination of optical transparency and outstanding mechanical properties. Moreover, their application in photonics, particularly with rare earth doping, has become prominent.

It is now well known that this is not universally achievable for all inorganic compounds and is significantly impacted by factors such as light scattering due to residual pores and the presence of secondary phases or impurities. Also, potential candidates for well-light-transmitting ceramics have to crystallize in the high-symmetry system (preferably in cubic). This group of materials is very limited, and taking into account non-doped and RE^{3+}-doped host lattices, it contains only garnets ($Y_3Al_5O_{12}$, $Lu_3Al_5O_{12}$), sesquioxides (Y_2O_3, Sc_2O_3,

and Lu$_2$O$_3$), spinels (MgAl$_2$O$_4$), fluorides (CaF$_2$), selenides (ZnSe), sulfides (ZnS), and perovskite-type BMT (Ba(MgZrTa)O$_3$), primarily utilized in lasers, scintillating materials, or solid-state lighting, as previously highlighted in our earlier publications.

For polycrystalline non-cubic ceramics, additional scattering losses due to birefringent splitting of the beam at grain boundaries occur. This scattering depends on the grain size and is smaller the smaller the grain size is (the grain size must be in the sub-μm range) [4].

Given the extensive research conducted on transparent ceramics, it was revealed that the incorporation of MgO, LiF, or SiO$_2$ as sintering aids can improve the transparency of sintered bodies [5–7]. For example, the groundbreaking fabrication of transparent ceramic Nd-doped yttrium aluminum garnet, Nd:YAG, was performed by Ikesue using SiO$_2$ as the sintering aid [8]. This cubic transparent ceramics has been demonstrated to be superior to its single-crystal counterpart for laser applications [9]. Nonetheless, certain transparent ceramics, such as MgAl$_2$O$_4$ spinel [10], Al$_2$O$_3$ [11,12], CaF$_2$ [13], and (La,Y)$_2$O$_3$ [14], can be crafted without employing a sintering aid. This is frequently achieved through a synergistic combination of appropriate initial powders and a densification process that imparts a substantial driving force to the sintering process, namely via techniques like Hot Isostatic Pressing (HIP), Hot Pressing (HP), or Spark Plasma Sintering (SPS) [15].

One of our research programs is focused on exploring novel materials (mainly cubic) with the potential to yield highly transparent optical ceramics from families other than those already known and applied. For example, our studies comprised cubic molybdates of Y$_6$MoO$_{12}$ [16], molybdato-tungstates of La$_2$MoWO$_9$ [17–19], tungstates (articles under review), and most recently, eulytite-type phosphates of Ba/Sr$_3$Y(PO$_4$)$_3$ [20], from which we have succeeded in obtaining some translucent ceramic bodies.

Current research involves different interesting phosphates characterized by high thermal and chemical stability, such as calcium phosphate. As it crystallizes in a hexagonal structure, the size and homogeneity of the initial powder are extremely important. The fabrication of transparent ceramics from non-cubic raw materials is possible, but their nanoparticles should be of the order of several tens of nanometers.

In the literature, one can find a few papers reporting studies on polycrystalline transparent ceramics based on phosphates from three groups: Ca$_3$(PO$_4$)$_2$ *β*-TCP [21], hydroxyapatite Ca$_{10}$(PO$_4$)$_6$(OH)$_2$ (HA) [22], and fluorapatite Ca$_{10}$(PO$_4$)$_3$F$_2$ (FAP) [23]. They crystallize in the trigonal (s. g., *R3c*, no. 111) and hexagonal (*P63/m*, no. 176) crystal systems, respectively. Among them, calcium phosphate transparent ceramics were considered a good candidate for storage phosphors in dosimetry and may also be applied as scintillators for *α*-ray detection [24], while fabricating transparent bio-compatible hydroxyapatite ceramics with nanosized grains is important for direct observations of in vivo interactions with proteins and/or cells [25,26].

In turn, the most important achievement for fluorapatites is a diode-pumped anisotropic (non-cubic) ceramic laser that uses microdomain-controlled Nd^{3+}-doped hexagonal fluorapatite (Nd^{3+}:Ca$_{10}$(PO$_4$)$_6$F$_2$, Nd:FAP) polycrystalline ceramics as the gain medium. They were fabricated by the RE^{3+}-assisted magnetic grain-orientation control method as a step toward achieving giant micro-photonics [27,28]. Furuse et al. demonstrated laser oscillation in randomly oriented non-cubic FAP ceramics activated with Nd^{3+} and Yb^{3+} ions [29,30].

All these transparent materials were obtained *via* advanced sintering techniques, i.e., SPS. Eriksson et al. conducted intriguing research, exploring the use of a high-pressure SPS approach to achieve transparency in SPS processes conducted at lower temperatures but under elevated pressure conditions [31]. However, none of these studies used sintering aids.

In this work, we chose non-cubic calcium phosphate as Ca$_{10}$(PO$_4$)$_6$(OH)$_2$ hydroxyapatite to investigate the effect of using different amounts of LiF on the quality of the obtained sintered body. LiF is a well-known sintering aid with a melting point of approximately 850 °C [2,3]. When utilized as an additive in the densification processes of ceramic materials, particularly in methods involving uniaxial pressure such as HP and SPS, LiF plays a crucial role. It manifests a distinctive capacity to generate a low-viscosity lubricating film upon compact particles. This film, in turn, facilitates the processes of particle sliding

and rearrangement, thereby creating enhanced densification through the mechanism of liquid-phase sintering. The use of LiF was particularly useful to obtain transparent ceramic materials of $MgAl_2O_4$ spinel [32], but also YAG [33], $Dy^{3+}:Y_2O_3$ [34], $Sm^{3+}:Y_2O_3$ [35], $Nd^{3+}:Lu_2O_3$ [36], and MgO [37].

The use of sintering additives may reduce the temperature, which is optimal for obtaining a transparent material; therefore, the effect of the temperature applied during the sintering on the quality of the sintered bodies was also checked.

From the articles of Kim et al. and Kato et al. [22,24], we know that the fabrication of transparent ceramics based on calcium phosphate is possible. However, the experiments described by the Japanese researchers used a commercially available powder from Japan, which is not accessible to us. As in the next stages of our project, we want to activate hydroxyapatite with rare earth ions, so optimizing the sintering conditions to obtain the highest quality transparent undoped host lattice was crucial. This is why we also checked the effect of the starting powder used for the process on the optical quality of our sintered specimens. All sintering procedures were performed via the SPS process, which is an efficient method of consolidating polycrystalline materials at relatively low temperatures in a short time.

2. Materials and Methods

2.1. Powders Used for Sintering via SPS Method

Two types of nanopowders, i.e., commercially available and synthesized by us, were used for sintering experiments. The commercially available powder was tricalcium phosphate $Ca_3(PO_4)_2 * \times H_2O$ (Sigma-Aldrich, St. Louis, MI, USA) with particle size <200 nm (BET), which was in reality hexagonal hydroxyapatite, as we will show in the next part. So, we named it in this paper COM. HA. The second nano-crystalline powder was obtained in our laboratory.

Here, it is necessary to mention that the literature is rich in reports on hydroxyapatite synthesis methods, particularly those employing hydrothermal [38,39] or precipitation reactions [40] as well as sol–gel techniques [41–43]. Microwave radiation has also been explored as a novel means to achieve higher purity and ultrafine-sized powders [44,45]. Additionally, innovative synthesis protocols, such as mechano-chemical synthesis [46] and surfactant-modified hydrothermal methods [47], have been explored.

We decided to fabricate nanopowdered hydroxyapatite *via* hydrothermal (HT) reaction following the protocol described in [48]. This laboratory-made powder is named in the paper as LAB. HA. For this synthesis, commercially available $Ca(NO_3)_2 * 4H_2O$ (Alfa Aesar, 99.98%) and analytically pure $NH_4H_2PO_4$ (Chempur, 99.5%) were used. Proper quantities of calcium nitrate and ammonium phosphate were individually dissolved in distilled water. The controlled addition of the $NH_4H_2PO_4$ solution to the $Ca(NO_3)_2$ solution, executed drop-wise with continuous stirring, led to the formation of a precipitate, achieving a targeted Ca/P ratio of 1.67. The initial pH of the suspension was approximately 5.1, but as a result of the gradual introduction of NH_4OH (Sigma-Aldrich, ACS reagent grade), the pH increased to achieve the desired value of 11.0. The addition of NH_4OH not only makes it possible to precise pH control, but it also serves to protect against carbonate formation during the synthesis process. After vigorous stirring for an additional 10 min, the solution was transferred into a Teflon-lined HT reactor and heated at 200 °C for 24 h. Under natural cooling to RT, the particulate product was collected through centrifugation. The collected powder underwent a thorough washing process involving repeated resuspension in distilled water and subsequent particle sedimentation through centrifugation at 6000 rpm for 5 min. This washing procedure was repeated five times, with a concluding methanol rinse to reduce feasible agglomeration in the final dried powder. The drying process was executed in an oven at 80 °C for 12 h.

2.2. Sintering by SPS

The samples were sintered using an SPS sintering machine, type FCT System HP D25, Rauenstein, Germany. The nanopowder of calcium phosphate was poured into a graphite die with an internal diameter of 10 mm. The die was surrounded with a 5 mm thick layer of graphite wool to ensure thermal insulation. The interior surface of the graphite die was lined with a 0.35 mm thick graphite foil. Temperature monitoring was facilitated by an axial pyrometer focused on a designated orifice positioned 3 mm above the material surface within the die. Pellets were produced under vacuum conditions, maintaining consistent powder quantities (0.5 g) inserted between the pistons in the die for all experiments. In some cases, the appropriate amounts of 0.25 to 1 wt.% of LiF (Alfa Aesar, 99.98%) were added to the initial powder and ground in an agate mortar using a small amount of ethanol. The sintering conditions used in numerous tests were similar in terms of pressure, moment of pressure application, temperature rise, and dwell time. However, the sintering temperature was modified. Initially, the temperature was increased from 20 to 750 °C for 30 min. under pressure of 38 MPa and kept at this temperature for 10 min. Subsequently, the temperature was raised from 750 °C to the expected temperature (950–1100 °C), respectively, while the applied axial pressure increased to 100 MPa. The temperature was held for 15 min while maintaining the applied pressure. Sintering was performed in a vacuum. Finally, the pressure was reduced to 38 MPa and the temperature to 950 °C in 10 min. Then the specimen was cooled to RT naturally. The sintering cycle of calcium phosphate powder was chosen based on the studies of Kim et al. [22] and. Kato et al. [24]. The sample thickness after sintering was in the range of 1.03–1.36 mm. Before characterization to eliminate any geometric imperfections and remove the carbon-contaminated layer resulting from contact with the graphite die and punch, both sides of the sintered pellets were polished, as described below. All samples were polished to the same thickness of approximately 1 mm.

2.3. Analysis and Characterization Techniques

Structural analysis and Rietveld refinements from X-ray powder diffraction data. The powder X-ray diffraction patterns for nanopowdered samples and micro-ceramics were recorded at RT using a Bruker D8 Advance X-ray diffractometer with Ni-filtered $CuK_{\alpha 1+2}$ radiation ($K_{\alpha 1+2}$, λ = 1.5418 Å). The step rate was 0.032° per step, and the counting time was 1.5 s per step within the range of 10–80° 2θ. The diffractograms were compared with the simulated XRD patterns of hexagonal $Ca_{10}(PO_4)_6(OH)_2$ (PDF 01-086-1203) and trigonal $Ca_3(PO_4)_2$ (PDF 00-70-2065), respectively. X-ray diffraction analyses were realized to check if the desired initial phases are present in the powder and that there is no phase decomposition during sintering. Also, it was checked whether the obtained specimens did not contain a trace of contamination by carbon originating from the graphite die.

The Rietveld refinements were performed for sintered bodies in order to determine the ratio between the two phases, i.e., hexagonal and trigonal, present in each sintered body. Calculations were performed using the HighScore Plus 3.0 software, with the initial parameters derived from crystal data of two phases: hexagonal $Ca_{10}(PO_4)_6(OH)_2$ s. g., *P63/m* no. 176 (COD #1011242) and trigonal $Ca_3(PO_4)_3$ s. g., *R3c*, no. 161 (COD #1517238). A determined background was used, and peak shapes were modeled using a pseudo-Voigt function. Global variables, specifically specimen displacement [mm], were refined for the obtained patterns. Structural parameters involved the scale factor and unit cell parameters. Peak profile variables were fine-tuned using "U left", "V left", and "W left" with respect to Peak Shape 1 Left. A crucial parameter for achieving well-refined results was the incorporation of preferred grain orientation during calculations. Due to the distinct crystal cell parameters (a and c) of the two phases, the intensities of XRD diffraction lines vary. Refining this parameter resulted in achieving low percentages of R_p and R_{wp} values (where R_p is the R profile and R_{wp} is the weighed profile), hence more precise phase ratios for the analyzed samples.

2.3.1. Microscopic Analysis of Starting Powders by TEM

To check the quality, particle size, and morphology of nanopowders used for sintering *via* SPS, the Transmission Electron Microscopy (TEM) technique was employed. The measurements were carried out on a H-8100 TEM of a Hitachi company (Tokyo, Japan) equipped with a Penta FET EDX detector (Oxford Instruments, UK). An acceleration voltage of 200 kV was applied. The nanopowders were suspended in ethanol, subsequently deposited onto a copper grid coated with carbon, and then dried in air.

2.3.2. Microscopic Analysis of Sintered Ceramics by SEM

All sintered bodies were investigated by scanning electron microscopy (SEM) using a Hitachi S-3400 N equipped with an energy-dispersive X-ray spectroscopy EDS detector, Thermo Scientific Ultra Dry. The observations were made in the secondary electron (SE) mode with a high voltage of 2.00 kV and a beamed current equal to 50 pA. The ceramic samples were not coated with any gold alloy layer; however, to perform these measurements, they were properly polished and annealed for 1h at a temperature 100 °C lower than the sintering one.

2.3.3. Disc Polishing

The polishing process proceeded in the following manner: first, diamond shields with grit sizes of 200, 500, 1200, and 4000 μm were employed. Then the diamond grains, suspended in a lubricating fluid, were applied to the polishing cloth with grit sizes of 5 μm, 3 μm, 1 μm, and 100 nm. The polishing effect was continuously controlled after each polishing cloth to obtain the best-quality mirror-faced polished samples.

2.3.4. Density Measurements

The density of the sintered samples was measured using Archimedes' method with distilled water. The values of the relative densities were calculated assuming a theoretical density of 3.13 g/cm^3 for the hexagonal phase and 3.14 g/cm^3 for the trigonal phase, and taking into account the ratio of both phases for each ceramics. The measurement uncertainty was ± 0.2.

2.3.5. Transmission Measurements of Sintered Ceramics

To evaluate the optical quality of the obtained polished ceramics, the total optical transmission of the specimens was measured at RT in the spectral region of 300–850 nm using an Edinburgh FLS980 spectrofluorometer, equipped with a 450 W xenon continuous arc lamp, R928P, R2658P PMT detectors, and an integrating sphere. The transmission was normalized to 1 mm thickness.

3. Results

3.1. Raw Nanopowder Characterizations

Before sintering, both powders, i.e., COM. HA and LAB. HA, were carefully investigated in terms of phase purity (XRD) and morphology (TEM).

3.1.1. Phase Analysis

The hexagonal crystal system is the most commonly occurring structure for hydroxyapatite. It is characterized by *P63/m* (no. 176) space group symmetry and lattice parameters of $a = b = 9.432$ Å, $c = 6.881$ Å, and $\gamma = 120°$. The structure comprises an arrangement of PO$_4$ tetrahedra, which are interconnected by Ca^{2+} ions scattered throughout. These Ca^{2+} are sited in two distinct crystal positions: in precisely aligned columns (Ca(I)) and within equilateral triangles (Ca(II)) that revolve around the screw axis. The OH groups are situated in columns on the screw axes, whereby neighboring OHs diverge in rival directions. It is important to note that such an arrangement suggests the existence of steric hindrance among the closest OHs. Hence, to inverse the direction of OH$^-$ within a column, it is

necessary to eliminate some of the OH⁻ to create reversal points. It may be achieved by substituting OH⁻ with a vacancy, F⁻, Cl⁻, or any suitable replacement [49].

β-TCP is a high-temperature phase that is typically obtained by thermal conversion of amorphous calcium phosphate and has the most stable tricalcium phosphate crystalline structure. This material was confirmed to have a rhombohedral structure (s. g., *R3c*, no. 161). Unit-cell parameters with higher precision ($a = b = 10.4352(2)$ Å, $c = 37.4029(5)$ Å, $\alpha = \beta = 90°$, and $\gamma = 120°$ in the hexagonal setting) and positional parameters for oxygen with equal precision were obtained by the neutron powder diffraction technique, compared with the single-crystal X-ray diffraction data by Dickens et al. [50]. The site Ca(4) with atomic coordinates (0.0, 0.0, −0.0851(6)) was confirmed to be very different from the other four Ca sites. The position Ca(4) is three-fold coordinated with oxygen atoms and has a lower occupancy factor of 0.43(4) and a higher isotropic thermal parameter. On the contrary, each of the Ca(1), Ca(2), Ca(3), and Ca(5) is fully occupied by one Ca atom, and these positions are coordinated with seven, eight, eight, and six oxygen atoms, respectively.

Both powders used for sintering represent a hexagonal crystal system. Figure 1 presents the XRD patterns acquired for COM. HA and LAB. HA nanopowders. The diffraction patterns show a big similarity between both samples.
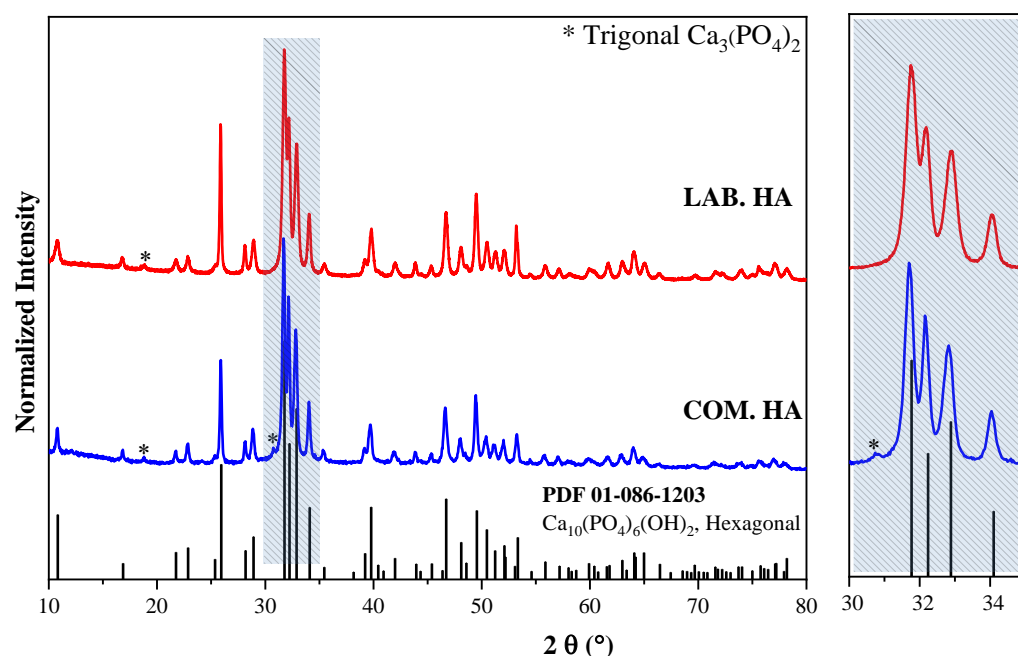

Figure 1. Powder XRD patterns of COM. HA and LAB. HA nano-crystalline calcium phosphates together with simulated PDF #01-086-1203 of hexagonal hydroxyapatite.

Reflexes within the 10–80 2θ range were identified and indexed to the hexagonal phase of Ca10(PO₄)₆(OH)₂ with s. g., *P63/m*. The wider reflexes, indicating smaller grains, are observed for the sample prepared in our laboratory. In turn, the diffraction patterns for the COM. HA display an additional line of very weak intensity at 30.5 2θ, corresponding to the trigonal phase of $Ca_3(PO_4)_2$. The studies show that the powder obtained by us is characterized by greater quality.

3.1.2. Morphology and Particle Size of Nanopowders by TEM Analysis

Using high-resolution TEM imaging, it was possible to determine the particle size of the investigated materials. As depicted in Figure 2, the micrographs of COM. HA and LAB. HA nanopowders exhibit big differences in the homogeneity, shape, and size of the nanopowder.
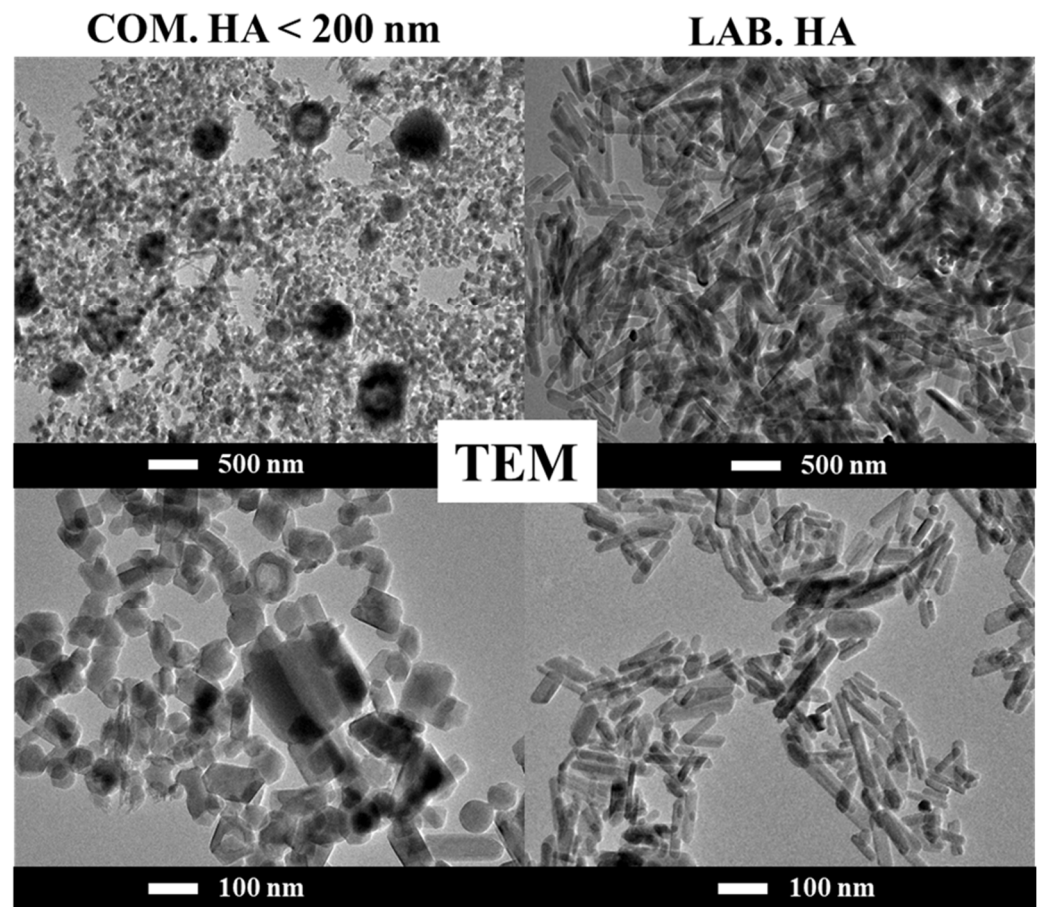
Figure 2. TEM image of COM. HA and LAB. HA nano-crystalline calcium phosphates.

The COM. HA possesses crystallites of different shapes, including spheres, rectangles, and ovals within the size range of 20–80 nm. The image obtained at low magnification shows that the material is quite homogeneous, the crystallites are well-separated from each other, and grain boundaries are clearly visible. However, spontaneously emerging agglomerates in the form of balls with a diameter of 200–500 nm are also visible. The micrographs shown in Figure S1 reveal the morphology of this nanopowder in detail. To check whether these agglomerates were not accidental, other commercially available powders were tested. The obtained results were identical. The elementary analysis by EDS (not presented here) was performed; however, it did not detect changes in the chemical composition of the big grains and the smaller ones. It is difficult to properly conclude why these large agglomerates are present in these commercially available powders.

In contrast, the LAB. HA demonstrates a significantly more homogeneous morphology without agglomerates in the form of balls. Nonetheless, the shape of the obtained crystallites is different; they form uniform rods with sizes ranging from 20 to 100 nm, as presented in detail in Figure S2.

The particle size distribution was analyzed more carefully. As can be seen in the histograms of both types of powder (Figure 3), the COM. HA powder in the majority is composed of particles with an average size of approximately 40 nm, while the sizes of the aggregates range from 175, 225, and 275 nm (marked with red arrows). For the nanopowders of LAB. HA, the particles in the form of rods reach an average size equal to 40–55 nm (length) and 19 nm (width). There is no doubt that LAB. HA nanopowder is more homogeneous.

(a) Commercial β-Ca$_3$(PO$_4$)$_2$ < 200 nm

(b) Ca$_5$(OH)(PO$_4$)$_3$ obtained *via* HT reaction
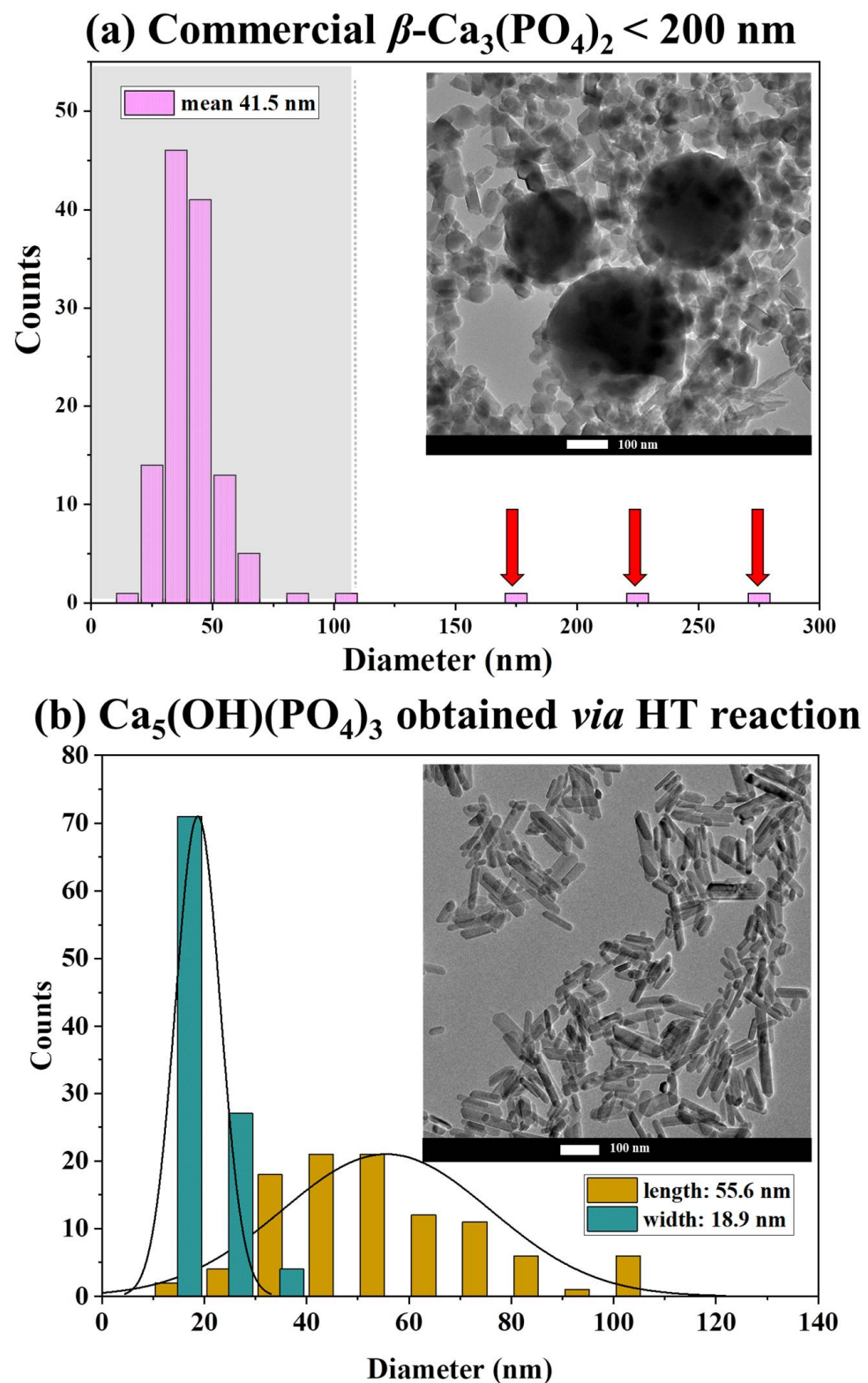
Figure 3. TEM images and particle size distribution of COM. HA (**a**) and LAB. HA (**b**).

3.2. Characterizations of Micro-Ceramics Fabricated by SPS

The current literature includes a few papers devoted to the fabrication of translucent and transparent polycrystalline ceramics based on tricalcium phosphate (β-TCP), hydroxyapatite (HA), and fluorapatite (FAP). Mainly, they are obtained by the SPS protocol, and the procedures exhibit variations in the applied sintering temperature, pressure, and dwell time.

Furthermore, different synthesis methods were employed to obtain the initial materials, resulting in sintered bodies differing in quality.

Here, the influence on the quality of sintered materials of changing parameters, such as: (a) application of the sintering additive LiF; (b) temperature used during SPS; and (c) starting materials, i.e., commercially available nanopowder synthesized by us *via* the HT method, were investigated and are described below.

3.2.1. Influence of LiF Doping

These experiments were performed using only COM. HA nanopowder. Different amounts of LiF (0.25–1 wt.%) were added to the initial powder and ground in an agate mortar using a small amount of ethanol. The sintering conditions used in the four tests were identical in terms of pressure, moment of pressure application, temperature rise, and dwell time.

The SPS experiments were conducted based on the protocol proposed by Kato et al. [24]. The effect of the addition of LiF on SPS-produced calcium phosphate is illustrated in Figure 4. The best optical quality was observed when 0.25 and 0.5% of LiF were used.
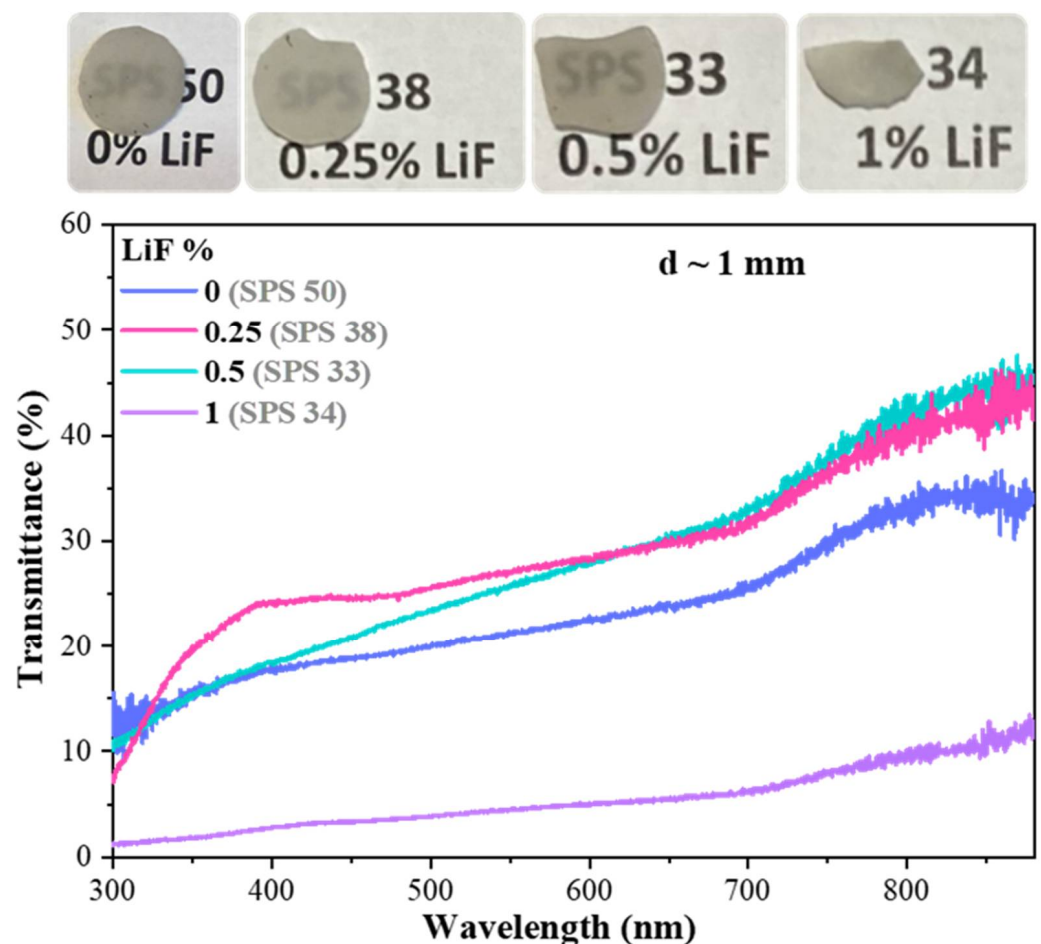

Figure 4. Photographs and total transmission spectra of translucent ceramics obtained by SPS at 1050 °C from COM. HA powder with different LiF contents. Transmittance normalized to ceramics' thickness = 1 mm.

The transmission spectra are similar, particularly within the infrared range of the spectrum, demonstrating a total transmittance of approximately 30% at 650 nm and 40–45% at 880 nm. Undoubtedly, the addition of LiF improves the quality and transmission of sintered bodies. However, when the concentration of the additive reaches 1 wt.%, the sample becomes completely opaque. This can be seen both in the photo and in the

graph presenting the transmission spectra. Sporadically occurring black spots are mainly caused by the penetration of carbon into the ceramics from the graphite die during the sintering process.

Figure 5 presents the images of the surfaces of ceramics obtained under the conditions described above. The most homogeneous morphology is observed for samples with 0.25% and 0.5% of LiF, which is consistent with the observed light transmission. Both samples possess well-compacted grains of spherical shapes, and the grain boundaries between the microcrystals are clearly seen. The average grain size in a sample with 0.25% LiF is equal to 2 µm, and possible pores appear very rarely. In the case of ceramics with 0.5% LiF, the average grain size is equal to 3 µm, but sometimes there are places where the grains are smaller, with a size of approximately 1 µm. The pores between grains are also more common. For the sample without sintering additive, the grains are the smallest, with an average size of 1 µm. In turn, the lack of transparency in the sample with 1% LiF is reflected in the least favorable morphology. The lost transparency of this sample can be attributed to the growth of large grains reaching even 8.5 µm and the lack of homogeneity.
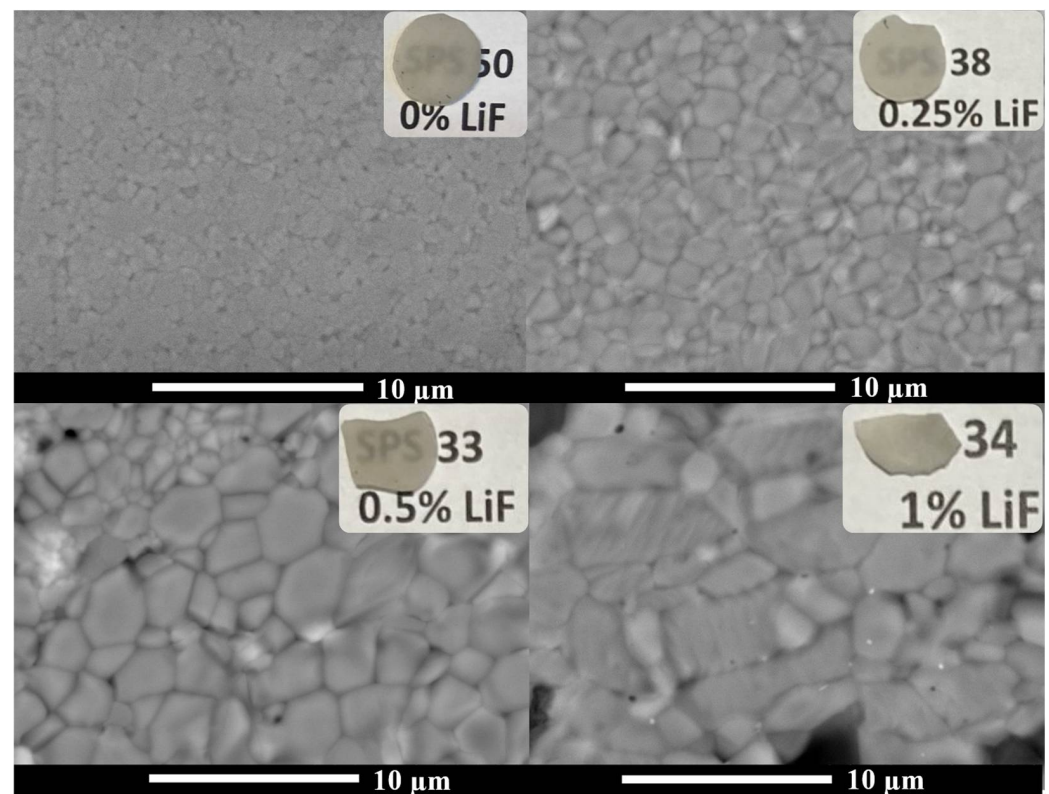
Figure 5. SEM micrographs of surfaces of ceramics obtained by SPS at 1050 °C from COM. HA nanopowder with different LiF contents.

The interesting and difficult-to-understand phenomenon, also observed but not discussed by Kato et al. [24], is the presence of two phases in all ceramics obtained as the result of the SPS process. Powder XRD patterns of all discussed here obtained by SPS at 1050 °C from COM. HA nanopowder with different LiF content are presented in Figure S3. Detailed information on the phase composition was gathered using Rietveld calculations. The ratio of HA to β-TCP varies depending on the percentage of LiF used. A rise in the hexagonal phase was observed with increasing LiF, and when 1% LiF was used, the amount of the hexagonal phase was close to 100%. However, in the case of the highest amount of hexagonal phase, the sintered body is completely opaque.

The values of relative densities range from 98.8 to 99.5%. The values for the samples containing 0.25% and 0.5% LiF are the lowest (98.8%). However, these two samples out of the four analyzed show the best light transmission. In the case of a sample with 1% LiF

(density 99.5%), a compact microstructure is observed, but the bigger grain size makes it impossible to obtain transparency. Table 1 summarizes all the results discussed above.

Table 1. Based on Rietveld calculations, phase compositions of ceramics sintered by SPS at 1050 °C from COM. HA nanopowder with different LiF content; grain size observed by SEM; values of total transmittance monitored at 650 and 880 nm (transmittance normalized to ceramics' thickness = 1 mm); and measured density.

| LiF wt. %	Phase 1—Main Ca$_5$(PO$_4$)$_3$(OH) Hexagonal *P63/m* (No 176) HA	Phase 2 Ca$_3$(PO$_4$)$_2$ Trigonal *R3c* (No 161) β-TCP	Grain Size (μm)	Transmission in % at 650 nm	Transmission in % at 880 nm	Relative Density %
0	71.4%	28.6%	0.41–2.1	23.4	33.8	99.0
0.25	77.7%	22.3%	0.55–3.2	29.7	42.8	98.8
0.5	81.8%	18.2%	2.1–5.4	30.5	45.6	98.8
1	94.5%	5.5%	1.8–8.5	5.5	12.8	99.5

3.2.2. Influence of Temperature of SPS

The next stage of the research was to check the effect of the temperature used during the SPS process. Based on the results described above, we decided to use 0.25 wt.% LiF as a sintering aid. All the tests were performed using COM. HA nanopowder. In the literature, one can find a few papers on ceramics made from calcium phosphates and their procedures using different sintering temperatures (remark to the correcting person: temperature is only valid in the singular) [22,24,25,34]. However, no additives were used in these studies. All experiments were carried out using the same sintering parameters; only the temperature was modified.

Figure 6 presents the photographs and total transmission spectra of translucent ceramic samples obtained by SPS at different temperatures from COM. HA powder is mixed with 0.25 wt.% of LiF as a sintering additive. The best optical quality was observed for the samples sintered at 1000 °C. Although the quality of the sample obtained at 1050 °C is also good, the worst results were obtained for the ceramics sintered at the lowest (950 °C) and highest (1150 °C) temperatures. Both samples are almost black due to the effect of contamination by carbon originating from the graphite die.

The specimen obtained at 1100 °C is also darker than the two best samples. Temperature is a key parameter that plays a huge role in the process of manufacturing transparent ceramics. The analysis of the morphology of ceramics (Figure 7) and their optical quality shows a strong correlation. The best and most homogenous morphology is observed for the samples obtained at 1000 °C and 1050 °C. The grains of spherical shapes are well-compacted, and pores are observed to be extremely rare. In both cases, the average grain's size is equal to 2 μm. The specimen obtained at 950 °C creates crystallites of the smallest sizes (~1 μm), but the morphology is not very homogenous. An increase in the temperature of the SPS process resulted in a proportional increase in average grain size to even 6 or 7 μm at the highest temperature, i.e., 1150 °C.

Powder XRD patterns of all ceramics obtained by SPS at different temperatures from COM.HA nanopowder with 0.25% LiF are presented in Figure S4. The analysis revealed, as previously, the presence of HA and β-TCP, while the starting powder initially exhibited an almost pure phase of HA. The ratio of these two phases stays more or less on the same level around 3 (HA): 1 (β-TCP), regardless of temperature (Table 2). Its changes are not as significant as they were observed when the amount of LiF varied. A slight increase in the content of the HA phase was notable up to a temperature of 1000 °C, and then the amount of this phase decreased slightly.
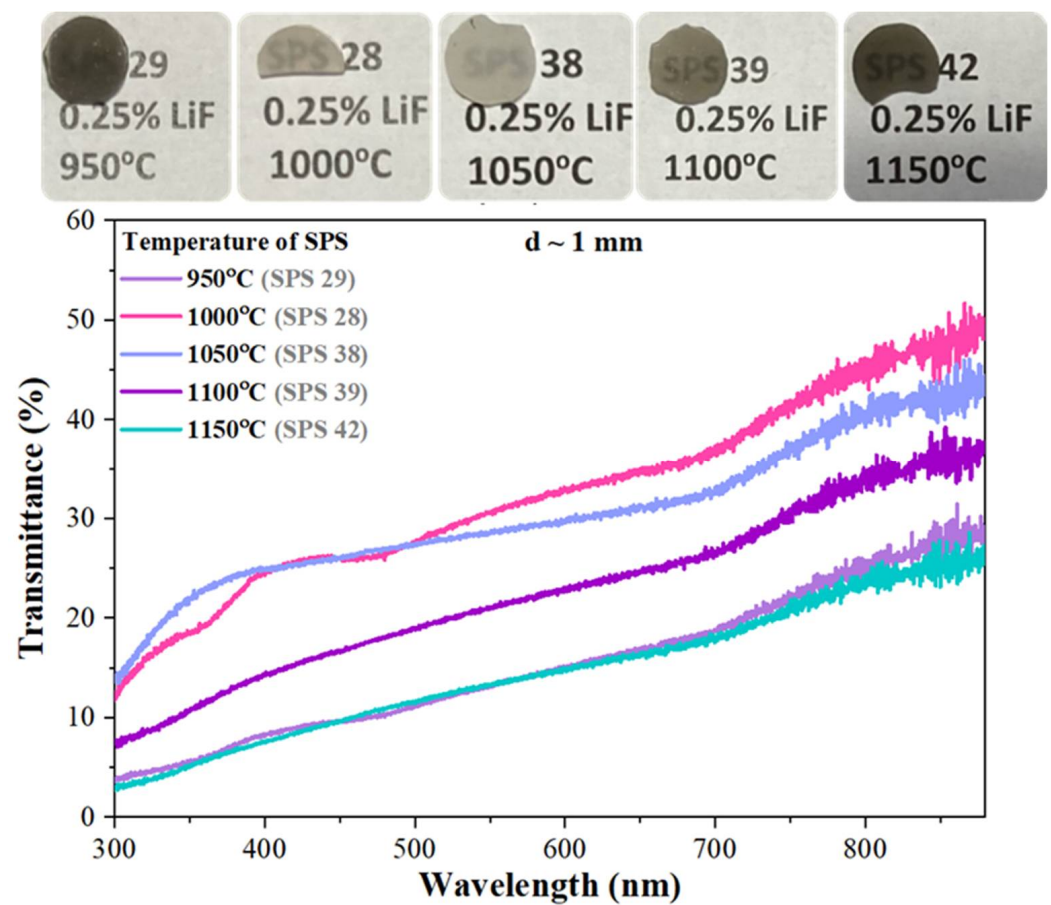
Figure 6. Photographs and total transmission spectra of ceramics obtained by SPS at different temperatures from COM. HA nanopowder with 0.25% LiF. Transmittance normalized to ceramics' thickness = 1 mm.

Table 2. Based on Rietveld calculations, phase compositions of ceramics sintered at different temperatures from COM.HA powder with 0.25% LiF; grain size observed by SEM; values of total transmittance monitored at 650 and 880 nm (transmittance normalized to ceramics thickness = 1 mm); and measured density.

Temperature of Sintering x °C/15 min	Phase 1—Main $Ca_5(PO_4)_3(OH)$ HA Hexagonal	Phase 2 $Ca_3(PO_4)_2$ β-TCP Trigonal	Grain Size (μm)	Transmission in % at 650 nm	Transmission in % at 880 nm	Relative Density %
950 °C	77.4%	22.6%	0.6–1.5	16.8	29.2	99.4
1000 °C	**79.3%**	**20.7%**	**0.7–2.6**	**34.8**	**48.7**	**99.3**
1050 °C	**77.7%**	**22.3%**	**0.55–3.2**	**29.7**	**42.8**	**98.8**
1100 °C	71.5%	28.5%	0.7–6.4	24.5	37.2	98.9
1150 °C	73.9%	26.1%	2.1–7.2	16.2	25.6	99.2

The values of measured densities range from 98.8 to 99.4%. The samples characterized by the best transmission of light and the best morphology show the highest density, as presented in Table 2.
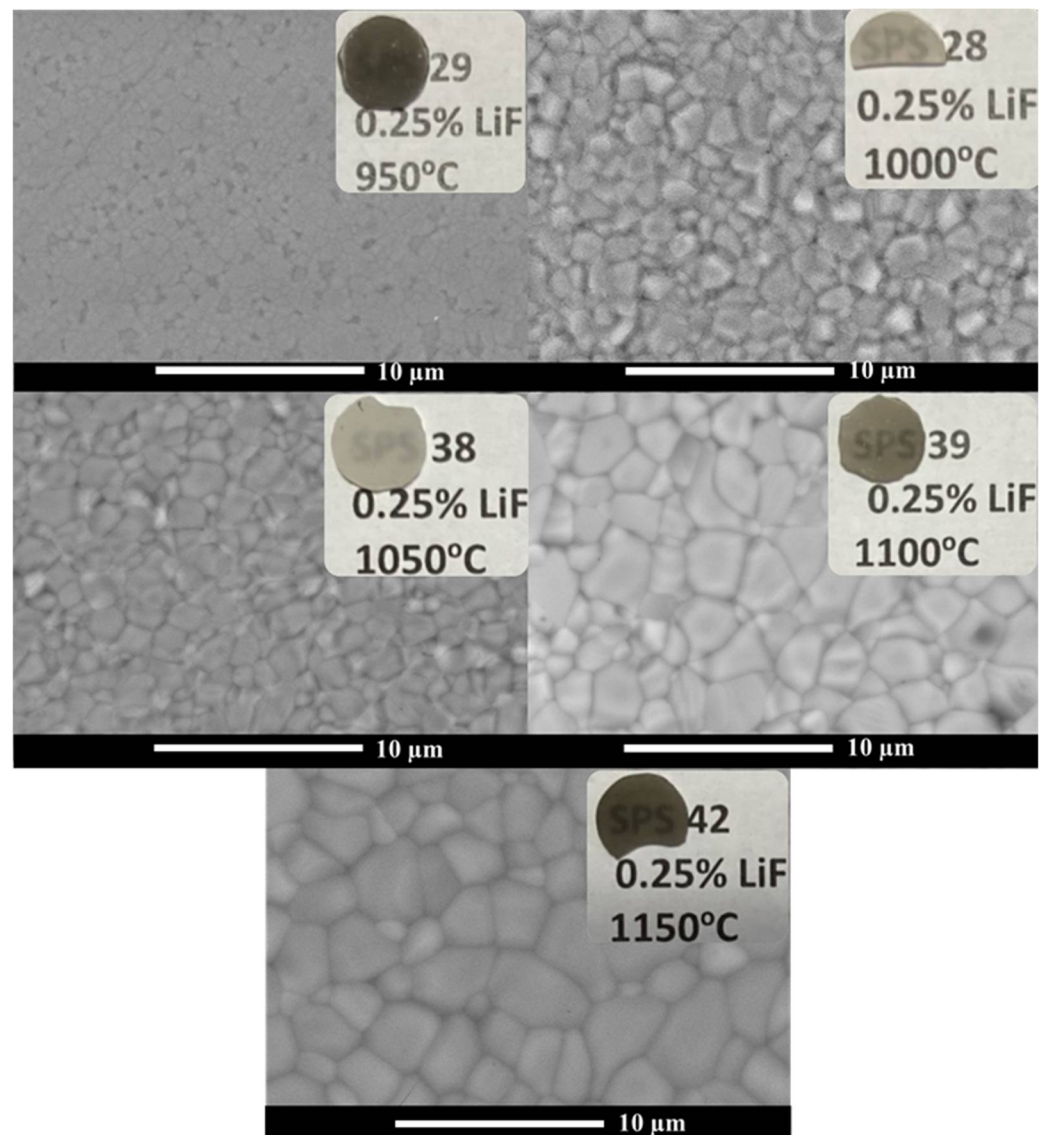
Figure 7. SEM micrographs of surfaces of ceramics obtained by SPS at different temperatures from COM.HA nanopowder with 0.25% LiF.

3.2.3. Influence of the Starting Material

According to the results presented above, the obtained sintered bodies did not exhibit the expected high level of transparency, similar to that which we could see in the reported papers [22,24]. The quality of the sintered specimens seems to be strongly influenced by the quality of the initial powder. All the experiments carried out by us, are based on the only calcium phosphate nanopowder available on our market.

So, taking into account our results indicating the optimal temperature and LiF content applied for the fabrication process, in the last step we decided to check how the starting materials influence the transparency of sintered materials. We prepared four samples from the nanopowdered hydroxyapatite synthesized in our laboratory by the hydrothermal method.

Two samples did not contain LiF, and the temperature of sintering was 1000 °C and 1050 °C, respectively. The next two were prepared at the same temperature, but using 0.25% LiF as a sintering aid.

Figure 8 presents photographs and total transmission spectra of translucent ceramic samples obtained by SPS from COM. HA and LAB. HA nanopowders. Without a doubt, it can be concluded that ceramics prepared from laboratory-made nanopowders are of much better quality and exhibit higher transparency. The sample from COM.HA powder without

LiF additive shows the worst light transmission, while the best specimens were obtained from LAB. HA with the addition of 0.25 wt.% LiF.
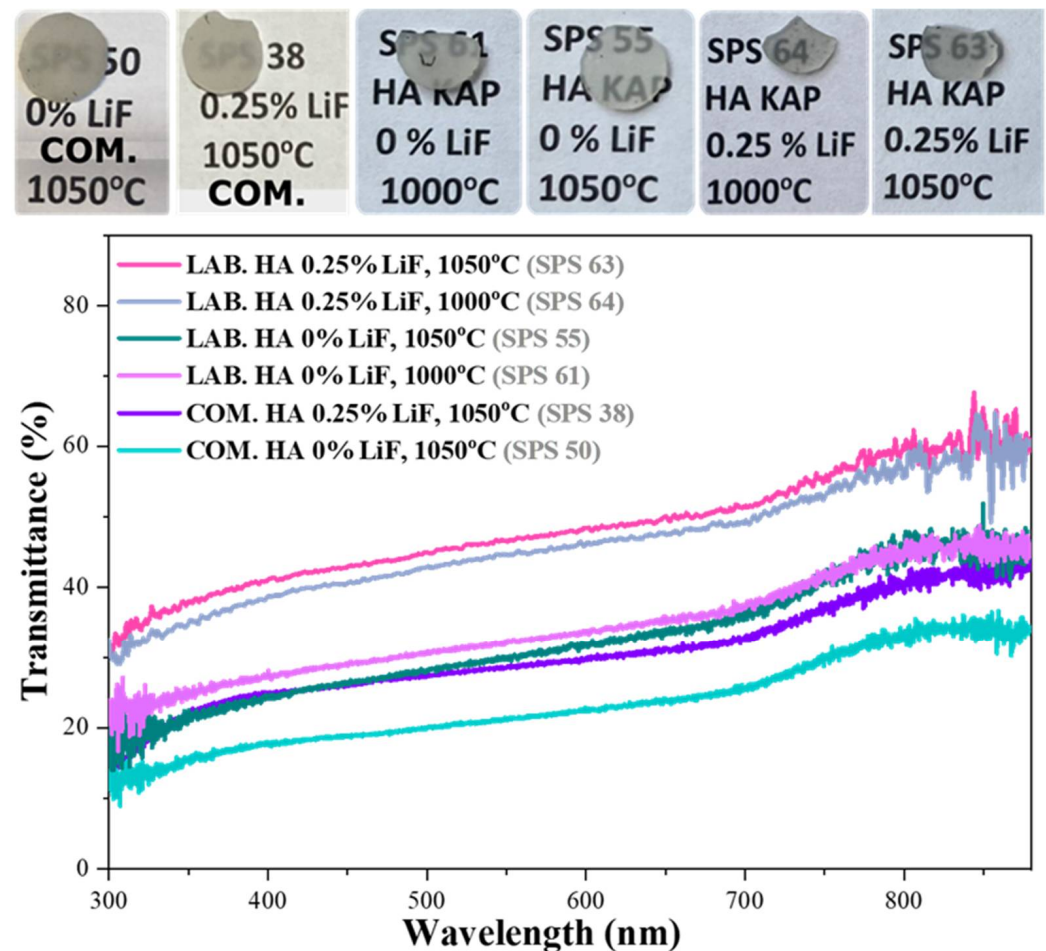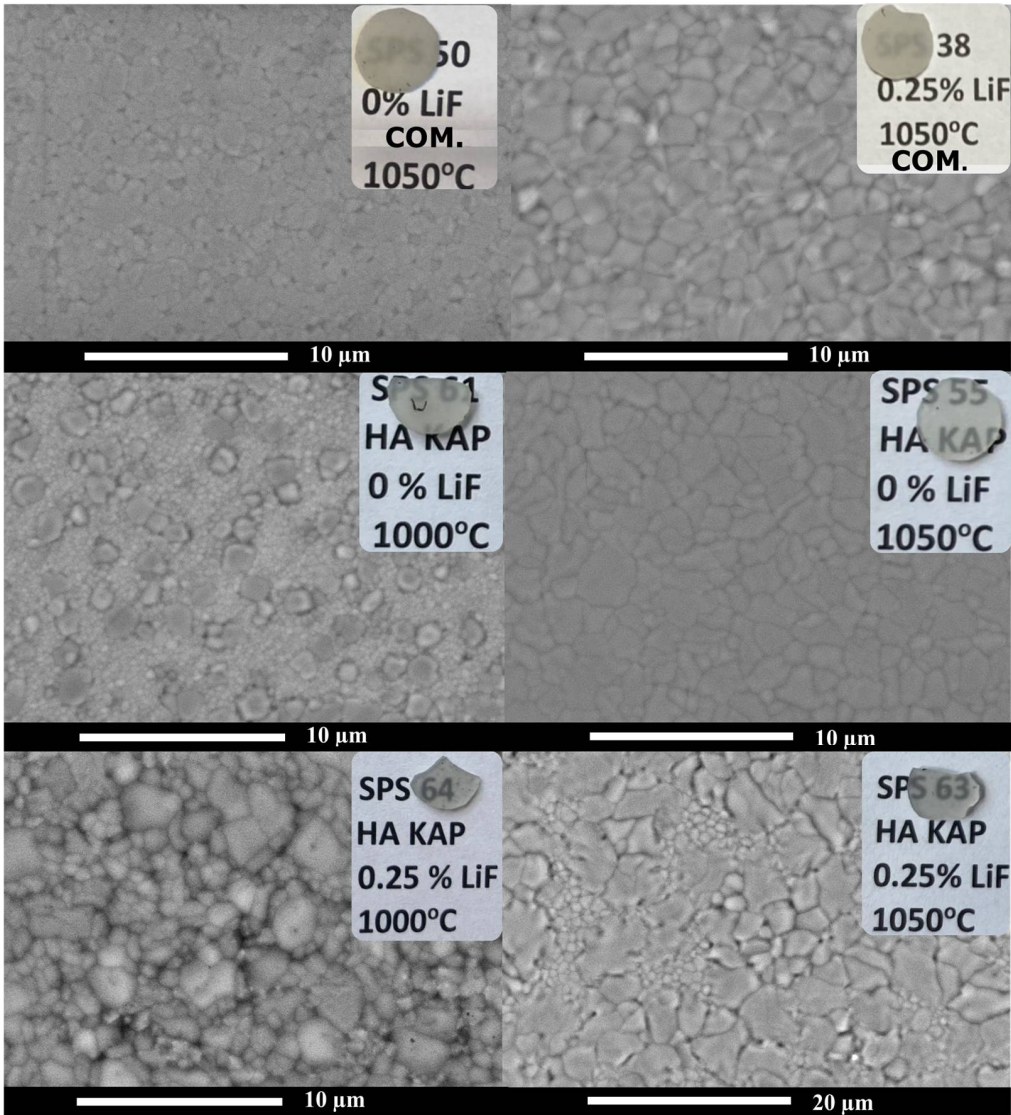

Figure 8. Photographs and total transmission spectra of ceramics obtained by SPS from COM. HA and LAB. HA nanopowders with and without the addition of LiF and sintered at 1000 °C or 1050 °C. Transmittance normalized to ceramic thickness = 1 mm.

Presented in Figure 9, SEM micrographs of surfaces of sintered bodies obtained from two different starting powders with and without the addition of LiF and sintered at 1000 °C or 1050 °C revealed that the temperature of 1000 °C applied for the sintering is too low or the time (15 min) is too short to obtain good homogeneity and uniform grain sizes. The sintered material consists of larger and smaller grains.

Powder XRD patterns of all ceramics obtained by SPS from COM. HA and LAB. HA nanopowders with and without the addition of LiF and sintered at 1000 °C or 1050 °C are presented in Figure S5. As previously stated, Rietveld's calculations (Table 3) made it possible to evaluate the ratio between HA and *β*-TCP phases present in all obtained ceramics. For the LAB. HA, the amount of hexagonal phase is higher than that calculated for specimens obtained from COM. HA powder, especially for both ceramics fabricated using 0.25 wt.% LiF, for which the values reach almost 90%. For these two samples, the highest values of transmission of light, almost 60%, were obtained.

In the case of the samples from two types of starting materials, the values of all measured densities are above 99%. The highest density was observed for the ceramics from LAB. HA with 0.25% LiF sintered at 1050 °C (Table 3), which corresponds to the best results obtained from SEM and transmission analysis (Figure S6).

Figure 9. SEM micrographs of surfaces of ceramics obtained by SPS from COM. HA and LAB. HA nanopowders with and without the addition of LiF and sintered at 1000 °C or 1050 °C.

Table 3. Based on Rietveld calculations, phase compositions of ceramics obtained by SPS from COM. HA and LAB. HA nanopowders with and without application of LiF and sintered at 1000 °C or 1050 °C; grain size from SEM; values of total transmittance monitored at 650 and 880 nm (transmittance normalized to ceramics' thickness = 1 mm); and measured density.

Starting Material	LiF wt. %	Temp. of SPS x °C/ 15 min	Phase 1 HA Hexagonal	Phase 2 β-TCP Trigonal	Grain Size (µm)	Transmission in % at 650 nm	Transmission in % at 880 nm	Relative Density %
COM. HA	0	1050 °C	70.3%	29.7%	0.48–2.1	24.1	34.4	99.0
	0.25		77.7%	22.3%	0.55–3.2	29.7	42.8	98.8
LAB. HA	0	1000 °C	87.2%	12.8%	0.29–0.35 / 0.9–1.5	35.3	45.9	100.2
		1050 °C	84.6%	15.4%	0.7–2.7	33.3	45.1	99.6
	0.25	**1000 °C**	**89.8%**	**10.2%**	**0.4–1** / **2.2–3.2**	**47.3%**	**59.1%**	**99.8**
		1050 °C	**89.4%**	**10.6%**	**0.5–0.8** / **2.4–5.0**	**50%**	**59.3%**	**99.9**

4. Conclusions

Two types of nanopowders, i.e., commercially available (COM. HA) and laboratory-made by us (LAB. HA) *via* the hydrothermal (HT) protocol, were used to fabricate non-cubic hydroxyapatite $Ca_{10}(PO_4)_6(OH)_2$-based microcrystalline ceramics. All sintering procedures were performed *via* the SPS process, which is an efficient method of consolidating poly-crystalline materials at relatively low temperatures in a short time. The effect of affected parameters such as the addition of LiF sintering agent, the temperature applied during the SPS process (in the range 950–1100 °C), and the quality of the starting nanopowders, on the optical quality of sintered ceramics were checked. XRD, microscopic (TEM and SEM) techniques, and light transmission measurements were used to characterize both the starting materials as well as the quality of the sintered samples. Highly transparent HA micro-ceramics were obtained from nano-crystalline powder obtained *via* the hydrothermal method. The addition of LiF as a sintering aid has a positive effect on the quality of ceramics when added in an amount of 0.25–0.5 wt.%, while the most favorable temperature for SPS sintering of this material was 1000–1050 °C for 15 min under 100 MPa pressure. These optimal conditions result in well-compacted dense micro-ceramics with a grain size of ~2–3 μm and transmission at 880 nm of ~60%. The research highlighted the crucial role of the quality of the starting materials on the quality and optical transparency of polycrystalline ceramics sintered by the SPS method. The values of measured densities stay in agreement with the results obtained from SEM analysis and measurements of light transmission.

Subsequent investigations toward enhancing transparency through the exploration of variations in applied pressure as well as the fabrication of HA ceramics doped by RE^{3+} ions are the subject of our present research.

References

1. Ikesue, A.; Aung, L.A. (Eds.) *Processing of Ceramics: Breakthroughs in Optical Materials*; Wiley: Hoboken, NJ, USA, 2021.
2. Goldstein, A.; Krell, A. Transparent ceramics at 50: Progress made and further prospects. *J. Am. Ceram. Soc.* **2016**, *99*, 3173–3197. [CrossRef]
3. Goldstein, A.; Andreas Krell, A.; Burshtein, Z. *Transparent Ceramics: Materials, Engineering, and Applications*; Wiley: Hoboken, NJ, USA, 2020; ISBN 978-1-119-42949-4.
4. Krell, A.; Hutzler, T.; Klimke, J. Transmission physics and consequences for materials selection, manufacturing, and applications. *J. Eur. Ceram. Soc.* **2009**, *29*, 207–222. [CrossRef]
5. Hostaša, J.; Picelli, F.; Hříbalová, S.; Nečina, V. Sintering aids, their role and behaviour in the production of transparent ceramics. *Open Ceram.* **2021**, *7*, 100137. [CrossRef]
6. Frage, N.; Cohen, S.; Meir, S.; Kalabukhov, S.; Dariel, M.P. Spark plasma sintering (SPS) of transparent magnesium-aluminate spinel. *J. Mater. Sci.* **2007**, *42*, 3273–3275. [CrossRef]
7. Nečina, V.; Pabst, W. Comparison of the effect of different alkali halides on the preparation of transparent $MgAl_2O_4$ spinel ceramics via spark plasma sintering (SPS). *J. Eur. Ceram. Soc.* **2020**, *40*, 6043–6052. [CrossRef]
8. Ikesue, A.; Kinoshita, T.; Kamata, K.; Yoshida, K. Fabrication and optical properties of high-performance polycrystalline Nd: YAG ceramics for solid-state lasers. *J. Am. Ceram. Soc.* **1995**, *78*, 1033–1040. [CrossRef]
9. Yagi, H.; Yanagitani, Y.; Takaichi, K.; Ueda, K.; Kaminskii, A. Characterizations and laser performances of highly transparent $Nd^{3+}:Y_3Al_5O_{12}$ laser ceramics. *Opt. Mater.* **2007**, *29*, 1258–1262. [CrossRef]
10. Talimian, A.; Pouchly, V.; El-Maghraby, H.F.; Maca, K.; Galusek, D. Transparent magnesium aluminate spinel: Effect of critical temperature in two-stage spark plasma sintering. *J. Eur. Ceram. Soc.* **2020**, *40*, 2417–2425. [CrossRef]
11. Grasso, S.; Yoshida, H.; Porwal, H.; Sakka, Y.; Reece, M. Highly transparent α-alumina obtained by low cost high pressure SPS. *Ceram. Int.* **2013**, *39*, 3243–3248. [CrossRef]
12. Kim, B.N.; Hiraga, K.; Morita, K.; Yoshida, H. Spark plasma sintering of transparent alumina. *Scr. Mater.* **2007**, *57*, 607–610. [CrossRef]
13. Sarthou, J.; Aballea, P.; Patriarche, G.; Serier-Brault, H.; Suganuma, A.; Gredin, P.; Mortier, M.; Riman, R. Wet-route synthesis and characterization of $Yb:CaF_2$ optical ceramics. *J. Am. Ceram. Soc.* **2016**, *99*, 1992–2000. [CrossRef]
14. Ivanov, M.; Kalinina, E.; Kopylov, Y.; Kravchenko, V.; Krutikova, I.; Kynast, U.; Li, J.; Leznina, M.; Medvedev, A. Highly transparent Yb-doped $(La_xY_{1−x})_2O_3$ ceramics prepared through colloidal methods of nanoparticles compaction. *J. Eur. Ceram. Soc.* **2016**, *36*, 4251–4259. [CrossRef]
15. Ikesue, A.; Aung, L.A.; Lupei, V. *Ceramic Lasers*; Cambridge University Press: Cambridge, UK, 2013.
16. Sobota, P.; Guzik, M.; Garnier, V.; Fantozzi, G.; Sobota, M.; Tomaszewicz, E.; Guyot, Y.; Boulon, G. Fabrication of Y_6MoO_{12} molybdate ceramics: From synthesis of cubic nanopowder to sintering. *Ceram. Int.* **2020**, *46*, 4619–4633. [CrossRef]
17. Wilk (Bieza), M.; Tomaszewicz, E.; Siczek, M.; Guyot, Y.; Boulon, G.; Guzik, M. The first characterization of cubic Nd^{3+}-doped mixed La_2MoWO_9 in micro-crystalline powders and translucent micro-ceramics. *J. Mater. Chem. C* **2022**, *10*, 10083–10098. [CrossRef]
18. Bieza, M.; Guzik, M.; Tomaszewicz, E.; Guyot, Y.; Lebbou, K.; Zych, E.; Boulon, G. Toward optical ceramics based on cubic Yb^{3+} rare earth ion-doped mixed molybdato- tungstates: Part I—Structural characterization. *J. Phys. Chem. C* **2017**, *121*, 13290–13302. [CrossRef]
19. Bieza, M.; Guzik, M.; Tomaszewicz, E.; Guyot, Y.; Lebbou, K.; Boulon, G. Toward optical ceramics based on cubic Yb^{3+} rare earth ion-doped mixed molybdate-tungstates: Part II—Spectroscopic characterization. *J. Phys. Chem. C* **2017**, *121*, 13303–13313. [CrossRef]
20. Prokop, K.A.; Siczek, M.; Tomaszewicz, E.; Rola, K.; Guyot, Y.; Boulon, G.; Guzik, M. Structural ordering studies of Nd^{3+} ion in cubic $M_3Y(PO_4)_3$ ($M = Sr^{2+}$ or Ba^{2+}) perovskites. First translucent ceramics from micro-crystalline cubic powders. *Ceram. Int.* **2024**, *50*, 8042–8056. [CrossRef]
21. Kawagoe, D.; Ioku, K.; Fujimori, H.; Goto, S. Transparent β-tricalcium phosphate ceramics prepared by spark plasma sintering. *J. Ceram. Soc. Jpn.* **2004**, *112*, 462–463. [CrossRef]
22. Kim, B.N.; Horiuchi, N.; Dash, A.; Kim, Y.W.; Morita, K.; Yoshida, H.; Ji-Guang, L.; Sakka, Y. Spark plasma sintering of highly transparent hydroxyapatite ceramics. *J. Jpn. Soc. Powder Powder Metall.* **2017**, *64*, 547–551. [CrossRef]
23. Furuse, H.; Kato, D.; Morita, K.; Suzuki, T.S.; Kim, B.N. Characterization of Transparent Fluorapatite Ceramics Fabricated by Spark Plasma Sintering. *Materials* **2022**, *15*, 8157. [CrossRef]
24. Kato, T.; Nakauchi, D.; Kawaguchi, N.; Yanagida, T. Optical and X-ray-induced luminescence properties of calcium phosphate of transparent ceramic form. *Sens. Mater.* **2020**, *32*, 1411–1417. [CrossRef]
25. Ioku, K.; Kamitakahara, M. Hydroxyapatite ceramics for medical application prepared by hydrothermal method. *Phosphorus Res. Bull.* **2009**, *23*, 25–30. [CrossRef]
26. Kotobuki, N.; Kawagoe, D.; Nomura, D.; Katou, Y.; Muraki, K.; Jujimori, H.; Goto, S.; Ioku, K.; Ohgushi, H. Observation and quantitative analysis of rat bone marrow stromal cells cultured in vitro on newly formed transparent β-tricalcium phosphate. *J. Mater. Sci. Mater Med.* **2006**, *17*, 33–41. [CrossRef]
27. Akiyama, J.; Sato, Y.; Taira, T. Laser ceramics with rare-earth-doped anisotropic materials. *Opt. Lett.* **2010**, *35*, 3598–3600. [CrossRef]

28. Akiyama, J.; Sato, Y.; Taira, T. Laser demonstration of diode-pumped Nd^{3+}-doped fluorapatite anisotropic ceramics. *Appl. Phys. Express.* **2011**, *4*, 022703-1–022703-3. [CrossRef]

29. Furuse, H.; Horiuchi, N.; Kim, B.N. Transparent non-cubic laser ceramics with fine microstructure. *Sci. Rep.* **2019**, *9*, 2–3. [CrossRef]

30. Furuse, H.; Okabe, T.; Shirato, H.; Kato, D.; Horiuchi, N.; Morita, K.; Kim, B.N. High-optical-quality non-cubic Yb^{3+}-doped $Ca_{10}(PO_4)_6F_2$ (Yb:FAP) laser ceramics. *Opt. Mater. Express* **2021**, *11*, 1756. [CrossRef]

31. Eriksson, M.; Liu, Y.; Hu, J.; Gao, L.; Nygren, M.; Shen, Z. Transparent hydroxyapatite ceramics with nanograin structure prepared by high-pressure spark plasma sintering at the minimized sintering temperature. *J. Eur. Ceram. Soc.* **2011**, *31*, 1533–1540. [CrossRef]

32. Rubat du Merac, M.; Kleebe, H.J.; Müller, M.M.; Reimanis, I.E. Fifty years of research and development coming to fruition; Unraveling the complex interactions during processing of transparent magnesium aluminate ($MgAl_2O_4$) spinel. *J. Am. Ceram. Soc.* **2013**, *96*, 3341–3365. [CrossRef]

33. Frage, N.; Kalabukhov, S.; Sverdlov, N.; Ezersky, V.; Dariel, M.P. Densification of transparent yttrium aluminum garnet (YAG) by SPS processing. *J. Eur. Ceram. Soc.* **2010**, *30*, 3331–3337. [CrossRef]

34. Hu, Z.; Xu, X.; Wang, J.; Liu, P.; Li, D.; Wang, X.; Zhang, J.; Xu, J.; Tang, D. Fabrication and spectral properties of $Dy:Y_2O_3$ transparent ceramics. *J. Eur. Ceram. Soc.* **2018**, *38*, 1981–1985. [CrossRef]

35. Hu, Z.; Xu, X.; Wang, J.; Liu, P.; Li, D.; Wang, X.; An, L.; Zhang, J.; Xu, J.; Tang, D. Spark plasma sintering of Sm^{3+} doped Y_2O_3 transparent ceramics for visible light lasers. *Ceram. Int.* **2017**, *43*, 12057–12060. [CrossRef]

36. Alombert-Goget, G.; Guyot, Y.; Guzik, M.; Boulon, G.; Ito, A.; Goto, T.; Yoshikawa, A.; Kikuchi, M. Nd^{3+}-doped Lu_2O_3 transparent sesquioxide ceramics elaborated by the Spark Plasma Sintering (SPS) method. Part 1: Structural, thermal conductivity and spectroscopic characterization. *Opt. Mater.* **2015**, *41*, 3–11. [CrossRef]

37. Jiang, N.; Xie, R.-J.; Liu, Q.; Li, J. Fabrication of sub-micrometer MgO transparent ceramics by spark plasma sintering. *J. Eur. Ceram. Soc.* **2017**, *37*, 4947–4953. [CrossRef]

38. Jokić, B.; Mitrić, M.; Radmilović, V.; Drmanić, S.; Petrović, R.; Janaćković, D. Synthesis and characterization of monetite and hydroxyapatite whiskers obtained by a hydrothermal method. *Ceram. Int.* **2011**, *37*, 167–173. [CrossRef]

39. Syukkalova, E.A.; Sadetskaya, A.V.; Demidova, N.D.; Bobrysheva, N.P.; Osmolowsky, M.G.; Voznesenskiy, M.A.; Osmolovskaya, O.M. The effect of reaction medium and hydrothermal synthesis conditions on morphological parameters and thermal behavior of calcium phosphate nanoparticles. *Ceram. Int.* **2021**, *47*, 2809–2821. [CrossRef]

40. Grigoraviciute-Puroniene, I.; Tsuru, K.; Garskaite, E.; Stankeviciute, Z.; Beganskiene, A.; Ishikawa, K.; Kareiva, A. A novel wet polymeric precipitation synthesis method for monophasic β-TCP. *Adv. Powder Technol.* **2017**, *28*, 2325–2331. [CrossRef]

41. Han, Y.; Li, S.; Wang, X.; Chen, X. Synthesis and sintering of nanocrystalline hydroxyapatite powders by citric acid sol-gel combustion method. *Mater. Res. Bull.* **2004**, *39*, 25–32. [CrossRef]

42. He, W.; Xie, Y.; Xing, Q.; Ni, P.; Han, Y.; Dai, H. Sol-gel synthesis of biocompatible Eu^{3+}/Gd^{3+} co-doped calcium phosphate nanocrystals for cell bioimaging. *J. Lumin.* **2017**, *192*, 902–909. [CrossRef]

43. Anee, T.K.; Ashok, M.; Palanichamy, M.; Kalkura, S.N. A novel technique to synthesize hydroxyapatite at low temperature. *Mater. Chem. Phys.* **2003**, *80*, 725–730. [CrossRef]

44. Han, J.K.; Song, H.Y.; Saito, F.; Lee, B.T. Synthesis of high purity nano-sized hydroxyapatite powder by microwave-hydrothermal method. *Mater. Chem. Phys.* **2006**, *99*, 235–239. [CrossRef]

45. Kalita, S.J.; Verma, S. Nanocrystalline hydroxyapatite bioceramic using microwave radiation: Synthesis and characterization. *Mater. Sci. Eng. C* **2010**, *30*, 295–303. [CrossRef] [PubMed]

46. Choi, D.; Kumta, P.N. Mechano-chemical synthesis and characterization of nanostructured β-TCP powder. *Mater. Sci. Eng. C* **2007**, *27*, 377–381. [CrossRef]

47. Bricha, M.; Belmamouni, Y.; Essassi, E.M.; Ferreira, J.M.F.; El Mabrouk, K. Surfactant-assisted hydrothermal synthesis of hydroxyapatite nanopowders. *J. Nanosci. Nanotechnol.* **2012**, *12*, 8042–8049. [CrossRef] [PubMed]

48. Bilton, M.; Milne, S.J.; Brown, A.P. Comparison of Hydrothermal and Sol-Gel Synthesis of Nano-Particulate Hydroxyapatite by Characterisation at the Bulk and Particle Level. *Open J. Inorg. Non Met. Mater.* **2012**, *2*, 1–10. [CrossRef]

49. Ma, G.; Liu, X.Y. Hydroxyapatite: Hexagonal or Monoclinic? *Cryst. Growth Des.* **2009**, *9*, 2991–2994. [CrossRef]

50. Dickens, B.; Schroeder, L.W.; Brown, W.E. Crystallographic studies of the role of Mg as a stabilizing impurity in β-$Ca_3(PO_4)_2$. The crystal structure of pure β-$Ca_3(PO_4)_2$. *J. Solid State Chem.* **1974**, *10*, 232–248. [CrossRef]